Numerical investigation of the burning characteristics of ventilation air methane in a combustion based mitigation system

[1*] D. Mira Martinez, [2]D. L. Cluff, [3]X. Jiang

[1] *CASE Department, Barcelona Supercomputing Center (BSC-CNS), Barcelona 08034, Spain*

[2] *College of Engineering, Mathematics and Physical Sciences, University of Exeter, Exeter EX4 4QF, UK*

[3] *Engineering Department, Lancaster University, Lancaster LA1 4YR, UK*

Abstract

Large-eddy simulation of the reacting flow field in a combustion-based mitigation system to reduce the emissions of methane contained in ventilation air methane is presented. The application is based on the preheating and combustion of ventilation air methane. Effects of preheating and methane concentration are examined in five computational cases. The results indicate that the oxidation of the ventilation air methane can take place in a co-annular jet configuration provided that the preheating temperature is as high as 500 K for mixtures containing a low methane concentration of 0.5%. It is found that the oxidation process that eventually leads to reaction and combustion is controlled by the methane concentration and the level of preheating.

Keywords: ventilation air methane (VAM), greenhouse gas (GHG), mitigation system, flameless oxidation, large-eddy simulation

1. Introduction

Methane is a greenhouse gas (GHG) with a global warming potential (GWP) that varies over the atmospheric residency time [1]. Upon release

*Corresponding author: daniel.mira@bsc.es (D. Mira Martinez)
Telephone number: +34 93 4054286

to the atmosphere and using a reference value of unity for carbon dioxide, the GWP is initially 56 over the first 20 years, 21 over 100 years and 6.5 over 500 years. The radiative forcing factor of methane is second only to that of carbon dioxide. These two attributes are central to the argument that methane released to the atmosphere has an immediate effect far more intense than that of the carbon dioxide release and could be responsible for creating a short-term high temperature perturbation or positive feedback loop [2, 3, 4]. Therefore, reduction of methane releases to the atmosphere is essential to minimize these global hazards. Besides, the absence of mitigation actions not only increases the global warming effect, but also has economical implications [5].

The atmospheric concentration of methane associated with coal mining is estimated to be about 15 % of the total anthropogenic methane produced, while coal handling, abandoned underground mines and surface mines represent about 26 % of the total emissions [6]. The largest fraction of atmospheric methane from coal mining activities is due to the release of ventilation air methane (VAM) [7]. Methods to mitigate VAM are desirable from a global climate perspective and could be economical if the energy contained in the ventilation flow is captured. Since methane is a high impact GHG, VAM from coal mining operations or abandoned mines should be targeted for mitigation and for the development of cost effective technologies for mitigation [8].

VAM has been difficult to exploit because it is a low methane concentration high volumetric flow case. A number of technologies have been developed to mitigate VAM and there are essentially two basic methods for the mitigation and utilization of VAM: ancillary and principal uses [9]. Ancillary use is referred to as the use of VAM as an oxidizer instead of ambient air in combustion engines, gas turbines or rotary kilns to improve combustion performance [10, 11]. When the VAM replaces air in a combustion process, it is employed as a secondary fuel residing in the intake air. Higher concentration sources of methane, such as drained sources are either flared or sold to the market [9]. The principal uses for VAM as a primary fuel can be found in thermal flow reverse reactors, catalytic flow reverse reactors, lean burn gas turbines (GTs), recuperative GT or regenerative thermal oxidation [12, 13]. In these instances, the VAM is oxidized when it comes in contact with ceramic beads or rock particles at a sufficiently high temperature. These systems usually require an external energy source to raise the temperature to the operating point and then it becomes sustainable as the VAM is consumed [14]. The addition of catalysts serves to reduce the oxidation temperature,

but catalysts are expensive and may require replacement.

Mitigation systems based on the oxidation of the low concentration methane contained in VAM mixtures have some potential for power generation [7]. A technology based on VAM oxidation, the VamTurBurner(C) currently being developed [7], uses waste heat from gas turbine exhaust to preheat the VAM and requires a second preheating stage, where energy is drawn from downstream by a heat exchanger or recirculation system to preheat the VAM further. This configuration allows a rise in temperature to a state such that the methane may be oxidized by an igniter flame. This new multi-generation system [7] uses the total heat from a cogeneration cluster, igniters and VAM as a heat source for the production of more electricity, industrial drying, hot water, heating or cooling. These thermal outputs of the multi-generation system might be available to other industries or to a community depending on proximity and demand. The preheating of the VAM is essential to the combustion process, since it contributes to flame stability and allows the ignition to take place under restrictive operating conditions and for ultra-lean mixtures.

The study of the combustion characteristics of ultra-lean mixtures is still at an early stage. Some groups have studied the combustion of ultra-lean hydrocarbon mixtures reporting the oxidation of the mixtures under certain conditions. A comprehensive analysis of the chemical kinetics involved in the ignition of ultra-lean methane for catalytic combustion was undertaken in the work by Wang et al [15] for the mixtures of interest here. Ignition in ultra-lean mixtures by extending the flammability limit has also been reported using subcritical microwaves [16] and preheating [17, 18]. The work by Cheng et al [19] showed that preheating extended the flammability limit for ultra-lean methane mixtures. The fuel oxidation takes place after the interaction with hot combustion products. Analysis of the flame structure for different mixtures and levels of flame stretch are found in the literature [20, 21]. It was reported that ignition was very sensitive to the amount of preheating, concentration and flame stretch. Simple flame configurations have been investigated using detailed chemistry in the literature [20, 21], but to the authors knowledge, the interaction of ultra-lean mixtures with a well-established turbulent flame has not been addressed.

This study aims to investigate the oxidation process and the dynamics of VAM mixtures interacting with the heat release at different preheating temperatures and methane concentrations for a simplified combustor configuration. The concept of large-eddy simulation (LES) is employed in the

present work and similar reacting conditions as those found in mild combustion [22, 23] are investigated here. The difference in this case is that there is no recirculation zone to mix reactants and products to achieve lean premixed conditions, since the lean homogeneous fuel mixture or VAM is directly supplied. The challenges of this configuration are associated with finding adequate operating conditions (preheating temperature and fuel concentration) for low concentration methane streams, so that VAM mixtures can be burnt in practical combustors.

This paper starts with an introduction of the background and motivation of the study. It is followed by the description of the governing equations and the theoretical aspects of the numerical strategy, while results for instantaneous and time-averaged flow fields are described and analyzed subsequently. Finally, some conclusions and directions for future work are also given.

2. Mathematical modeling

The analysis of the combustion dynamics of mixtures containing different methane concentrations is addressed here using large-eddy simulation. In LES, the large-scale structures of the flow are resolved by governing equations, while the small-scales are modelled using closure rules [24]. The flow field is filtered in space using a box filter given by $\Delta = V^{1/3}$, where V represents the cell volume.

In order to reduce the complexity of filtering variables with density variations, a Favre-averaged filtering is employed [25]. The filtering process is given by $\tilde{f} = \overline{\rho f}/\overline{\rho}$, where ' $\bar{\cdot}$ ' is used for space-filtered quantities and ' $\tilde{\cdot}$ ' for Favre-averaged variables. The LES governing equations for multi-species reacting compressible flows are presented in the next section, which include the conservation of mass, momentum, energy and species mass fractions respectively.

2.1. LES governing equations

The filtered governing equations for LES are given by:

$$\frac{\partial \overline{\rho}}{\partial t} + \frac{\partial (\overline{\rho}\widetilde{u}_j)}{\partial x_j} = 0 \tag{1}$$

$$\frac{\partial (\overline{\rho}\widetilde{u}_i)}{\partial t} + \frac{\partial (\overline{\rho}\widetilde{u}_j\widetilde{u}_i)}{\partial x_j} = -\frac{\partial \overline{p}}{\partial x_i} + \frac{\partial \overline{\tau}_{ij}}{\partial x_j} - \frac{\partial \tau_{ij}^{sgs}}{\partial x_j} \tag{2}$$

$$\frac{\partial(\overline{\rho}\widetilde{e})}{\partial t} + \frac{\partial(\overline{\rho}\widetilde{u}_j\widetilde{e})}{\partial x_j} = -\overline{p}\frac{\partial\widetilde{u}_j}{\partial x_j} - \frac{\partial\overline{q_j}}{\partial x_j} + \overline{\tau}_{ij}\frac{\partial\widetilde{u}_i}{\partial x_j} - \frac{\partial h_j^{sgs}}{\partial x_j} + \Theta^{sgs} + \overline{\dot{Q}^c} \quad (3)$$

$$\frac{\partial(\overline{\rho}\widetilde{Y}_m)}{\partial t} + \frac{\partial(\overline{\rho}\widetilde{u}_j\widetilde{Y}_m)}{\partial x_j} = \frac{\partial}{\partial x_j}(\overline{\rho}\overline{D}_m\frac{\partial\widetilde{Y}_m}{\partial x_j}) - \frac{\partial\Phi_{j,m}^{sgs}}{\partial x_j} + \overline{\dot{\rho}_m^c} \qquad m = 1, ..., N \quad (4)$$

where $\overline{\rho}$, t, $\widetilde{u}_i$, x_i, $\overline{p}$, $\overline{\tau}_{ij}$, $\widetilde{e}$, $\overline{q}_i$, $\dot{Q}^c$, $\widetilde{Y}_m$ and $\overline{\dot{\rho}}_m^c$ are the density, time, ith velocity component with $i = 1, 2, 3$ in Cartesian coordinates, pressure, stress tensor, internal energy, heat flux, combustion heat release, species mass fraction and the source term due to chemical reactions respectively. The index $m = (1 \text{ to } N)$ denotes the individual species, while the superscript sgs refers to the subgrid scale terms coming from the filtering process.

The filtered stress tensor $\overline{\tau}_{ij}$ is obtained neglecting the effect of the unresolved field [26] and is given by:

$$\overline{\tau}_{ij} = \overline{\mu}\left[(\frac{\partial\widetilde{u}_i}{\partial x_j} + \frac{\partial\widetilde{u}_j}{\partial x_i}) - \frac{2}{3}\frac{\partial\widetilde{u}_k}{\partial x_k}\delta_{ij}\right] \quad (5)$$

where μ represents the dynamic viscosity and δ_{ij} is the Kronecker delta. The temperature-dependent viscosity $\mu(T)$ is obtained from the Sutherland's law [27], while the filtered heat flux $\overline{q}_j$ is given by:

$$\overline{q}_j = -\overline{K}\frac{\partial\widetilde{T}}{\partial x_j} + \overline{\rho}\sum_{m=1}^{N}\widetilde{h}_m\overline{D}_m\frac{\partial\widetilde{Y}_m}{\partial x_j} \quad (6)$$

where $\overline{K}$, $\widetilde{T}$, $\overline{D}_m$, and $\widetilde{h}_m$ are the filtered thermal conductivity, temperature, diffusion coefficient and enthalpy of species m respectively. The heat conductivity is obtained by providing a constant Prandtl number for each species contained in the flow field $K = \mu c_p/Pr$, while the equivalent diffusion coefficient of the mth species into the mixture D_m used in the calculations is obtained as [25]:

$$D_m = \frac{1 - Y_m}{\sum_{k\neq m}^{N} X_k/D_{km}} \quad (7)$$

where c_p is the heat capacity at constant pressure obtained from JANAF tables for a multi-component mixture and X_k is the species mole fraction of the kth species.

The subgrid scale terms τ_{ij}^{sgs}, h_j^{sgs}, Θ^{sgs} and $\Phi_{j,m}^{sgs}$ represent the unresolved momentum transport, the unresolved heat flux, the subgrid scale dissipation term and the subgrid scale species mass flux respectively. Note that the velocity-pressure gradient correlation term is neglected from the energy equations because of its negligible contribution to the energy equation. The subgrid scale diffusive mass flux was also neglected from the species conservation equations for the same reason [28].

The filtered reaction rates given in Arrhenius form are modelled without distinguishing between the resolved and unresolved scales. The reaction rates have been expressed in terms of the filtered variables and the effects of the subgrid scale motions are not considered in the reaction rates. The results are expected to provide estimations of the scalar fields that can be further improved by using a more precise reaction rate filtering approach.

The subgrid scale momentum transport is modelled using a one-equation model proposed by Menon et al [29] including the subgrid scale turbulent kinetic energy k^{sgs}. This model is known to account for the local non-equilibrium between energy production and dissipation. The subgrid scale stress τ_{ij}^{sgs} in the momentum equation is modelled using the turbulent viscosity $\nu_t = C_\nu \sqrt{k^{sgs}}\Delta$, while the unresolved stress is obtained as:

$$\tau_{ij}^{sgs} = -2\nu_t\big(\tilde{S}_{ij} - \frac{1}{3}\tilde{S}_{kk}\delta_{ij}\big) + \frac{2}{3}\overline{\rho}k^{sgs}\delta_{ij} \tag{8}$$

where C_ν is a constant set to be 0.067 [26], $\tilde{S}_{ij}$ is the filtered strain rate and the subgrid turbulent kinetic energy k^{sgs} is obtained after solving the following transport equation:

$$\frac{\partial \overline{\rho}k^{sgs}}{\partial t} + \frac{\partial \overline{\rho}\tilde{u}_j k^{sgs}}{\partial x_j} = -\tau_{ij}^{sgs}\frac{\partial \tilde{u}_i}{\partial x_j} + \frac{C_\varepsilon \overline{\rho}(k^{sgs})^{3/2}}{\Delta} + \frac{\partial}{\partial x_j}\Big(\frac{\overline{\rho}\nu_t}{Pr_t}\frac{\partial k^{sgs}}{\partial x_j}\Big) \tag{9}$$

where Pr_t is the turbulent Prandtl number set as 1.0 and C_ε is a model constant set as 0.916 [26].

The heat flux in the subgrid scale h_j^{sgs} as well as the subgrid scale species mass flux $\Phi_{j,m}^{sgs}$ are both modelled using a gradient diffusion approach [25]:

$$h_j^{sgs} = -\overline{\rho}\frac{\nu_t c_p}{Pr_t}\frac{\partial \widetilde{T}}{\partial x_j} \tag{10}$$

$$\Phi_{j,m}^{sgs} = -\overline{\rho}\frac{\nu_t}{Sc_t}\frac{\partial \widetilde{Y}_m}{\partial x_j} \tag{11}$$

where Sc_t is the turbulent Schmidt number. The subgrid scale viscous work Θ^{sgs} in the energy equation is given by:

$$\Theta^{sgs} = \frac{C_\varepsilon \overline{\rho}(k^{sgs})^{3/2}}{\Delta} \tag{12}$$

2.2. Chemical kinetics

The four-step reduced mechanism proposed by Jones and Lindsted [30] is employed here to account for the chemical kinetics involved in the oxidation of methane. The reduced chemical scheme was derived based on the analysis of the flame structure showing good agreement with experimental data when compared for flame speed, flame thickness and species profiles within the flammability regime [30, 31, 32]. The assessment of the chemical scheme employed in the numerical simulations is undertaken by comparing the predictions of flame temperature for methane in the ultra-lean regime with the detailed mechanism GRI-mech 3.0 [33], which contains 53 species undergoing 325 reactions. The results were compared using the code PREMIX [34] and the predictions in the ulta-lean regime with a preheating temperature of 500 K are acceptable as shown in Fig. 1.

The chemical kinetic mechanism involves four reversible chemical reactions comprising seven species (CH_4, CO_2, O_2 , CO, H_2O, H_2 and N_2) and is summarised in Table. 1.

Table 1: 4-step reduced kinetic mechanism for CH_4/O_2 oxidation.

	Reaction
I	$CH_4 + 1/2\ O_2 \rightleftharpoons CO + 2H_2$
II	$CH_4 + H_2O \rightleftharpoons CO + 3H_2$
III	$H_2 + 1/2\ O_2 \rightleftharpoons H_2O$
IV	$CO + H_2O \rightleftharpoons CO_2 + H_2$

2.3. Numerical methods

The Favre-averaged governing equations for a compressible multi-species flow are solved using a parallel code based on the finite-volume approach. The equations are solved in two stages allowing an implicit solver for the diffusion, and an explicit quasi-second order upwind scheme for the advection [35]. The code has been validated and compared to experimental data in a previous

study [28], where details of the parallel efficiency and the numerical schemes were also provided.

3. Application setup

This study aims to examine the feasibility of burning a stream of VAM by an existing flame in order to reduce the emissions of global warming gases. The VAM is usually released to the atmosphere because existing technologies still have difficulty making use of the methane contained in the VAM flow [7]. As a result, about 70 % of the methane emissions of the mine occurs as VAM and are released to the atmosphere without any treatment or processing. A mitigation system capable of burning the low methane concentration stream not only produces benefits from the reduction of the global warming potential of the VAM, but also provides an alternative local energy source. The objective of this work is to provide some insights into the conditions required for the oxidation of these mixtures as well as the flame dynamics under conditions of interest for practical applications. The following sections describe the computational domain and the computational cases selected to address this application.

3.1. Computational domain

The computational domain chosen to study the oxidation process of a VAM mixture corresponds to a simple jet flame configuration in which the low concentration fuel is injected as a reacting co-flow. Provided a jet flame is already established in the combustor, the VAM stream is oriented toward the combustor surrounding the flame in a duct configuration. The configuration is shown in Fig. 2, where three main regions can be identified. The grey region in the right-hand side plot of Fig. 2 corresponds to a real-sized combustion chamber and the blue zone embedded in it is the computational domain used for the simulations. The primary fuel injection pipe used to burn the VAM mixture can be distinguished in the left-hand side plot of Fig. 2. The domain represents only a small portion of the required mitigation systems allowing an accurate study of the unsteady reacting flow by large-eddy simulation. This configuration permits the investigation of the ignition of the VAM at the boundary of the established jet flame and the subsequent oxidation of the VAM stream. This is considered a preliminary test for more sophisticated and appropriate configurations such as annular burners with swirling effects that improve the mixing and combustion [36, 37].

A non-polar mesh system is used to represent the cylindrical computational domain. The radial direction is of a diameter D = 16.0 cm, which was proved to be sufficient to allow the flame spreading for all the computational cases, while the domain length was set as $H = 20.0$ cm to study the near field of the flow. The computational domain also includes a 0.3 cm section of the inlet channel of the primary fuel (see Fig. 2).

The nozzle of the primary fuel supply to develop a diffusion flame (also referred here as primary flame) has a diameter of $d = 0.45$ cm with a bulk velocity of 5000.0 cm/s. The secondary fuel supply (VAM mixture) has a bulk velocity of 135 cm/s (0.5-2.0 % CH_4 + 99.5-98.0 % Air) and comes in from an annular duct with an external diameter of D = 16.0 cm.

The boundary conditions considered in this problem are non-slip for the inner wall of the primary fuel nozzle with a diameter d = 0.45 cm (see Fig. 2), while continuative outflow conditions are specified at the downstream and azimuthal boundaries of the domain. A top-hat velocity profile is specified at the inlet of the primary fuel and the VAM co-flowing mixture.

A convergence analysis was addressed to evaluate and select a suitable mesh for this problem. Three different meshes with 1.4, 1.2 and 1.0 million cells were tested for this purpose simulating the methane flame used to ignite the VAM mixture with a co-flowing air. The results for the time-averaged streamwise velocity at three axial locations are presented in Fig. 3. The results show some minor differences between the meshes investigated at capturing the peak values; however, the trends are well predicted in all three cases. Considering the efficiency and accuracy in the numerical simulations, the mesh with 1.2 million elements is used throughout the study.

3.2. Computational cases

Five computational cases are considered in this study to evaluate some suitable conditions for which VAM mixtures can be burnt in practical applications. For a simple jet flame configuration and the VAM mixture issued as a reacting co-flow, the five computational cases presented in Table 2 are investigated. These cases are selected to evaluate the effects of methane concentration and the VAM preheating temperature on the combustion dynamics of this simple mitigation system. Cases A, B and C are 1.0% methane with the preheating temperature of 300 K, 400 K and 500 K respectively. Maintaining a constant methane concentration with increasing preheating temperature serves to benchmark the effect of increasing preheating. Case D and E are the lowest and highest methane concentrations of 0.5 % and 2.0 %

respectively and are subject to the highest preheating temperature, as that in Case C, of 500 K. Cases C, D and E serve to benchmark the effect of high preheating as the methane concentration increases.

Table 2: Computational cases.

Name	CH_4 concentration	Preheating temperature
Case A	1.0 %	300 K
Case B	1.0 %	400 K
Case C	1.0 %	500 K
Case D	0.5 %	500 K
Case E	2.0 %	500 K

4. Results

The results of the large-eddy simulations of the computational cases described above are presented in this section. The results are divided into two separate subsections: instantaneous results in which flame dynamics and vortical structures can be observed and time-averaged results for which mean variables and general trends are examined.

4.1. Instantaneous results

Instantaneous temperature contour plots at the middle plane Y = 0 of the domain for the five computational cases are presented in Fig. 4. It is observed that for a VAM mixture of 1.0 % CH_4, the oxidation of VAM only takes place after the gas is preheated up to 500 K. In this case, the existence of a primary flame is observed, which acts as a source of ignition for the VAM mixture and the formation of a flameless oxidation zone in the co-flowing VAM.

No substantial differences can be discerned between the flow dynamics in Cases A and B and the flow field is rather similar in both cases. However, the last snapshot in Case B displays some evidence of the initiation of local oxidation of the VAM mixture in the region surrounding the core of the primary flame. Combustion in this region is initiated at the reacting shear layer between the two streams and is largely affected by advective effects. The temperature of the VAM mixture is increased by the heat released by

the jet flame inducing the VAM oxidation. It is seen that after some time, partial ignition with combustion at low temperature might occur.

After further increasing the preheating temperature (Case C), the VAM mixture oxidizes as soon as the mixture enters the domain establishing a stable and uniform low temperature reaction zone upstream near the nozzle exit. The primary flame seems to be unaffected and the oxidation of the VAM mixture develops homogeneously downstream without showing significant interactions. The analysis of Cases A, B and C, demonstrates the effect of increasing preheating temperature on a VAM flow of constant methane concentration. It is shown that increasing the preheating temperature of the incoming VAM flow has a strong impact on the ignition mechanism of the VAM mixture causing the oxidation despite the relatively low concentration of the VAM.

The effects of increasing the methane concentration can be observed by comparing Cases C and D with E. It is observed that for ultra-lean methane mixtures, the preheating temperature has a strong impact on the oxidation mechanism of the mixtures, while the fuel concentration largely affects the flow field. For the conditions under investigation, the flammability limit of the VAM has been extended substantially by preheating the mixture leading to the oxidation of the three mixtures. Nevertheless, the fuel concentration at high temperature could lead to unstable flames as shown in Case E. In Cases C and D, the flame front has a smooth profile, which is evidence of flameless oxidation, while Case E shows a vortical flame front in the VAM stream at higher temperature. This reacting layer diffuses more heat to the preheating zone creating hot spots and inducing vortical structures (see the 0.03 s Case E cross section in Fig. 4). The heat released induces large density variations and strong pressure gradients leading to a more vortical and unstable flame. The dynamics of Case E are more complex than any of the lower methane concentration cases. As the methane concentration increases, an enhanced flame spreading is observed due to the influence of thermal conduction, oxidation of fuel in a CH_4-rich environment and the formation of dynamic vortical structures. Case D shows that the low methane concentration of the VAM can be oxidized provided that a sufficiently preheated flow exists. Because a smaller amount of methane is consumed in Case D, the reacting zone progresses slower than that of Case C. However, higher preheating conditions at high methane concentration may lead to unsteady flames (see Case E in Fig.4) and potential blow off.

The distribution of the methane concentration over the domain can also

be used to further understand the combustion dynamics of the VAM mixtures. Figure 5 shows the CH_4 mass fraction for the five computational cases at given time instant with a purple arrow added to represent the distance travelled by the VAM stream at that time instant. From Figs. 4 and 5, it can be deduced that there is no methane oxidation in Cases A and B, while for Case C, the methane at upstream location is mostly consumed. The absence of methane at upstream locations provides clear evidence of the flameless oxidation surrounding the primary reacting zone. This can be seen in Fig. 6 where a zoomed view of the profiles of methane mass fraction is shown at two axial locations. It indicates that the methane contained in the VAM of Cases A and B did not interact with the primary flame, while it was mostly consumed in the other cases. The primary flame tends to push the cold VAM mixture radially, although as the preheating increases, the two streams become closer until the oxidation takes place.

Time series analysis of data for temperature located at selected monitoring points near the flame core in the reacting zone can be used to investigate the ignition timing of the mixtures. Table 3 describes the location of the monitoring points. The time evolution of temperature at two locations (P1 and P2) close to the VAM inlet for the given mixtures is presented in Fig. 7. Cases A and B show that there is no reaction of the VAM mixture with the primary reaction zone, although the VAM stream in Case B is slightly heated. The temperature evolution for Case C indicates a low temperature oxidation after a delay for which the temperature of the VAM rises up to 800 K. Case D shows a similar evolution to Case C, but with a larger reaction initiation at a lower temperature due to the lower methane concentration. Finally, Case E is characterised by some oscillatory behaviour of temperature with time, which is caused by the increase of the oxidation reaction rate at the boundary of the primary reacting zone and throughout the VAM flow. This oscillatory behaviour is mainly induced by the local rapid burning of methane and the replacement of the fluid parcel by air.

Table 3: Location of the monitoring points.

Monitoring points	Location (x,y,z) [cm]
P1	$(3.0, 0.0, 0.5)$
P2	$(5.0, 0.0, 0.5)$

Profiles of temperature and species mass fractions also provide some important information about the dynamics of these flames. These are presented in Figs. 8 and 9 by means of radial profiles at two different streamwise locations. Upstream (see Fig. 8), it is observed that the temperature peaks are found in the shear layer of the primary flame and no substantial differences can be found among the mixtures. The effects of preheating and methane concentration in the VAM have shown to have a low impact on the dynamics of the primary flame, except in Case E. This case shows an increase in flame thickness that is not observed in the other cases, which is caused by the enlargement of the reacting shear layer of the flame by the fuel content of the oxidizer.

The carbon dioxide mass fraction profile shows that its concentration is highly influenced by the initial methane concentration. This demonstrates that small differences in the methane concentration in the VAM mixture have a strong impact on the production of carbon dioxide and act as a good confirmation that the desired methane oxidation reaction occurs. At downstream locations, the radial temperature distribution at Z = 4.0 cm contains several peaks caused by the fast oxidation of the VAM mixture. These peaks are associated with the enlarged flame shear zone and correspond to the unsteady flames as seen for Case E.

4.2. Time-averaged results

The time-averaged results presented in this section are obtained after two flow through calculations and time-integrated for another two flow through times. These data are used to statistically determine the mean values of the flow fields. The results are separated in two categories in order to study independently the effects of preheating and methane concentration on the burning characteristics of VAM mixtures.

The effects of preheating the mixture can be observed in Fig. 10 for Cases A, B and C. The profiles show that the preheating enhances the oxidation process because the energy level of the mixture is close to its activation energy; thus the heat required to oxidize the mixture is substantially reduced. It is observed that higher preheating temperatures lead to increased burning rates, since the flame becomes larger and the reaction zone enlarges.

The flame length is shorter and the flame spreading increases for high preheating temperatures due to the oxidation of the co-flowing VAM. The plot showing the combustion product CO_2 clearly indicates the location of the flame front and shows the large spreading experienced by the flame in Case

C. Note that the plots on the right-hand side of Fig. 10 show asymmetric results indicating that the time integration might need to be extended to achieve statistically fully converged results, although it would not affect the trends described here.

The effects of methane concentration at the fixed preheating temperature of 500 K can be examined by considering Cases C, D and E as shown in Fig. 11. For the higher concentration VAM mixtures, the flame length reduces substantially. Above a concentration of 1 % methane, most of the methane contained in the co-flow mixture burns producing large amounts of carbon dioxide. Combustion of the high methane concentrated flow also provides more heat by conduction, which assists the burning of the incoming VAM. The peak values of CO_2 production by the flames seem to be rather similar in all cases with methane concentration above 1 %. This difference, observed in the bottom-right plot of Fig. 11, is caused by the flame shortening experienced by Case E, where a large unsteady and vortical flame is formed after the VAM oxidation.

4.3. Study of the mixing process

In this section, the concept of unmixedness is introduced and examined for the mixtures under investigation. The temporal unmixedness is a factor used to describe the degree of mixing between fluid streams [38, 39] and is obtained following Fric et al. [40] as:

$$Z_{unmix} = \frac{Y_f'^2}{\overline{Y}_f(1-\overline{Y}_f)} \tag{13}$$

where $Y_f'^2$ represents the standard deviation obtained from the instantaneous fuel concentration field and $\overline{Y}_f$ is the average fuel concentration at that location. Note when Z_{unmix} is zero, the fuel is completely mixed and homogeneously distributed, while there is no mixing when Z_{unmix} is equal to unity. Values of Z_{unmix} close to unity would indicate large fluctuations of fuel mass fraction and shear mixing. The examination of the unmixedness factor at different axial locations shown in Figs. 12 and 13 provides some information concerning the mixing process between the primary flame and the VAM mixture.

The results corresponding to the cases with preheating temperature variation are shown in Fig. 12. Case A shows high degree of mixing between the primary fuel and the VAM stream with strong oscillations in the jet core.

This high level of shear mixing is caused by the interaction of the injection of the primary fuel with its surroundings leading to large peaks in the unmixedness profile. As the preheating temperature increases and the VAM stream approaches to ignition, the oscillations of the unmixedness become smaller, accordingly the mixing by fluctuations becomes less effective. The profiles of Case C indicate that the heat release after combustion smoothes out the fluctuations and therefore the peaks for Case C become smaller than for Case B as observed downstream (right-hand side plot of Fig. 12). The preheating temperature enhances the mixing process by reducing the unmixedness oscillations and facilitating the chemical reactions.

The effects of methane concentration on the mixing process are presented in Fig. 13 by means of profiles of the unmixedness factor Z_{unmix} at two axial locations. As already described, the largest mixing oscillations are found in the jet core region where the mixing of the primary flame takes place. The case with lower methane concentration of the VAM mixture (Case D) shows the largest variations. At upstream locations, no major differences are found between Cases C and E, and it is downstream where the differences become more evident. At Z = 4.0 cm, the flow field in Case E is more vortical and dynamic leading to large variations of unmixedness. The concentration of methane in the VAM stream has an influence on the magnitude of the unmixedness factor, but its effects on the distribution along the flame are rather low.

5. Conclusions

A numerical investigation, using large-eddy simulation, of a key process in a proposed VAM mitigation system to reduce methane emissions from mining activities has been performed. The mitigation device is based on the oxidation of a preheated VAM mixture by means of a primary fuel injection acting as a pilot or primary flame. The VAM mixture is supplied as a co-flowing stream and after the interaction with the heat release of the primary flame, it is oxidized provided certain conditions are achieved. The effects of preheating temperature and methane concentration are examined in five computational cases. It was found that the preheating temperature has a significant influence on the oxidation process of VAM mixtures. For a relatively low methane concentration stream, combustion only takes place when the temperature of the mixture is as high as 500 K. In this case, the oxidation of the mixture takes place homogeneously at low temperatures sur-

rounding the primary flame and a reaction zone over a large volume can be distinguished. At the higher methane concentration of 2.0 %, the heat released by the VAM oxidation tends to induce instabilities leading to strong oscillations. Preheating of the incoming VAM allows oxidation at methane concentrations as low as 0.5 %. Ignition timings are described and discussed for the different mixtures providing some insight into the flame dynamics in each case. Discussions of the flame structure and mixing evolution are also presented based on time-averaged results for the main reactants and products as well as the unmixedness parameter.

This study shows that the ventilation air methane flow oxidizes under certain conditions and motivates further analysis of the combustion characteristics of such mixtures for power generation. Mitigation systems to reduce greenhouse gas releases are extremely important from a global climate change perspective and further efforts from combustion researchers are required for the development of these systems.

6. Acknowledgements

The authors would like to thank the European Union's Research Programme of the Research Fund for Coal and Steel (RFCS) research programme under grant agreement number RFCR-CT-2010-00004 and EPSRC grant EP/G062714/2 for funding the activities undertaken for this study.

[1] Shine KP, Fuglestvedt JS, Hailemariam K, Stuber N, Alternatives to the global warming potential for comparing climate impacts of emissions of greenhouse gases, Climatic Change 2005;68:281-302.

[2] Shakhova N, Semiletov I, Methane release and coastal environment in the East Siberian Arctic shelf, J Marine Syst 2007;66:227-243.

[3] Isaksen ISA, Gauss M, Myhre G, Walter Anthony KM, Ruppel C, Strong atmospheric chemistry feedback to climate warming from Arctic methane emissions, Global Biogeochem. Cycles 2011;25,GB2002.

[4] Wickland KP, Striegl RC, Neff JC, Sachs T, Effects of permafrost melting on CO_2 and CH_4 exchange of a poorly drained black spruce lowland, J Geophys Res 2006;111:2156-2202.

[5] Whiteman G, Hope C, Wadhams P, Vast costs of Arctic change, Nature 2013;499:401-403.

[6] Kirchgessner DA, Piccot SD, Masemore SS, An Improved Inventory of Methane Emissions from Coal Mining in the United States, Journal of the Air & Waste Management Association 2000;50:1904-1919.

[7] Cluff DL, Kennedy GA, Bennett JG, Capturing Energy from Ventilation Air Methane, World Mining Congress, Montreal, Canada, 2013.

[8] Su S, Jenny A, Catalytic combustion of coal mine ventilation air methane, Fuel 2006;85:1201-1210.

[9] Su S, Beath A, Guo H, Mallett C, An assessment of mine methane mitigation and utilisation technologies, Prog Energ Combust 2005;31:123170.

[10] Wilson DG, Korakianitis T, The Design of High-Efficiency Turbomachinery and Gas Turbines, Prentice Hall, 2nd Edition (1998).

[11] Su S, Pohl JH, Holcombe D, Hart JA, A comparison of thermal condition between pilot- and full-scale furnaces for studying slagging and fouling propensity in PF boilers, Combust Sci Technol 2001;165:12950.

[12] Danell R, Nunn J, Kallstrand A, Demonstration of MEGTEC Vocsidizer for methane utilisation, ACARP Report C9065, Brisbane;2002.

[13] Cimino S, Pirone R, Russo G, Thermal stability of perpvskitebased monolithic reactors in the catalytic combustion of methane, Ind Chem Res 2001;40:805.

[14] Yin J, Li M, Zhu A, Zhu J, Part-load performance characteristics of a lean burn catalytic combustion gas turbine system, Journal of Thermal Science 2013;22:159-167.

[15] Wang Y, Liu Y, Cao Q, Wang Q, Che D, Homogeneous combustion of fuel ultra-lean methaneair mixtures: Experimental study and simplified reaction mechanism, Energ Fuel 2011;25:3437-3445.

[16] Michael J, Miles R, Ultra-lean combustion sustained by pulsed subcritical microwaves, 42nd AIAA Plasmadynamics and Lasers Conference;2011.

[17] Yahagi Y, Nihei H, Extinction and flame front behavior of ultra lean premixed flame formed in opposite flow, Transact Japan Society of Mechanical Engineers Series B; 2002;68:1287-1294.

[18] Hamatsu K, Yahagi Y; Takeuchi M, Nakahara S, Effects of oxidizer preheating and dilution on the Extinction and structure of CH4-O2-Ar diffusion flames, Transactions of the Japan Society of Mechanical Engineers Series B; 2006;72:1052-1059.

[19] Cheng Z, Wehrmeyer JA, Pitz RW, Lean or ultra-lean stretched planar methane/air flames, Proc Combust Inst 2005;30:59-66.

[20] Law CK, Proc. Combust. Inst. 22 (1988) 13811402.

[21] Barlow RS, Karpetis AN, Frank JH, Chen J-Y, Combust Flame 127 (2001) 21022118.

[22] Duwig C, Stankovic D, Fuchs L, Li G, Gutmar E, Experimental and numerical study of flameless combustion in a model gas turbine combustor, Combust Sci Tech 2008;180:279295.

[23] Coelho PJ, Peters N, Numerical simulation of a mild combustion burner, Combust Flame 2001;124:503-518.

[24] Pitsch H, Large-eddy simulation of turbulent combustion. Annu Rev Fluid Mech 2006;38:45382.

[25] Poinsot T, Veynante D, Theoretical and Numerical Combustion, R. T. Edwards, 2nd Edition (2005).

[26] Menon S, Calhoon W, Subgrid mixing and molecular transport modeling for large-eddy simulation of turbulent reacting flows, Proc Combust Inst 1996;26:59-66.

[27] Law CK, Combustion Physics, Cambridge University Press (2006).

[28] Mira Martinez D, Jiang X, Moulinec C, Emerson DR, Numerical simulations of turbulent jet flames with non-premixed combustion of hydrogen-enriched fuels, Comput Fluids 2013;88:688-701.

[29] Menon S, Yeung P-K, Kim W-W, Effect of subgrid models on the computed interscale energy transfer in isotropic turbulence, Comput Fluids 1996;25:165-180.

[30] Jones WP, Lindstedt RP, Global reaction schemes for hydrocarbon combustion, Combust Flame 1988;73:233-249.

[31] Abani N, Ghoniem AF, Large eddy simulations of coal gasification in an entrained flow gasifier, Fuel 2013;104:664-680.

[32] Ridhaa E, Mohamedb H, Rachida S, Comparison of different chemical kinetic mechanisms of methane combustion in an internal combustion engine configuration, Therm Sci 2008;12:43-51.

[33] Smith GP, Golden DM, Frenklach M, Moriarty NW, Eiteneer B, Goldenberg M, Bowman CT, Hanson RK, Song S, Gardiner WC, Lissianski Jr VV, Qin Z, http://www.me.berkeley.edu/gri_mech/.

[34] Kee RJ, Dixon-Lewis G, Warnatz J, Coltrin ME, Miller JA, A Fortran Computer Code Package for the Evaluation of Gas-Phase Multicomponent Transport Properties, Sandia National Laboratories, Report SAND86-8246;1986.

[35] Torres DJ, Trujillo MF, KIVA-4: An unstructured ALE code for compressible gas flow with sprays, J Comput Phys 2006;219:943-975.

[36] Jiang X, Luo KH, de Goey LPH, Bastiaans RJM, van Oijen JA, Swirling and impinging effects in an annular nonpremixed jet flame, Flow Turbul Combust 2010;86:63-88.

[37] Mira Martinez D, Jiang X, Large-eddy simulations of unsteady hydrogen annular flames, Comput Fluids 2013;80:429-440.

[38] Kang DM, Culick FEC., Ratner A, An experimental study of coupling between combustor pressure, fuel/air mixing, and the flame, 4th Joint Meeting of the U.S. Sections of the Combustion Institute;2005.

[39] Zheng Y, Zhu M, Mira Martinez D, Jiang X, Large-eddy simulation of mixing and combustion in a premixed swirling combustor with synthesis gases, Comput Fluids 2013;88: 702-714.

[40] Fric TH, Effects of Fuel-Air Unmixedness on NOx Emissions, J Propul Power 1993;9:708-713.

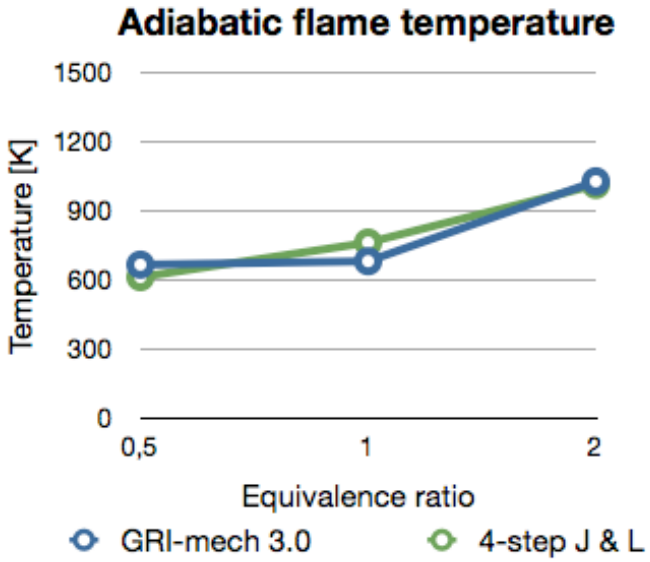

Figure 1: Comparison of the four-step reduced mechanism with the GRI-mechanism 3.0.

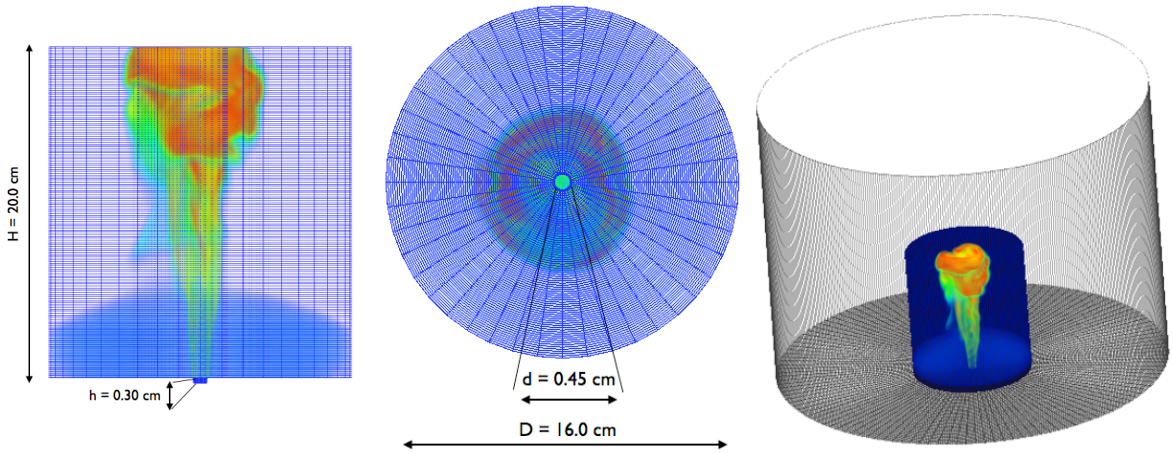

Figure 2: Description of the computational domain (left and middle plots) and embedded domain in a realistic configuration (right plot).

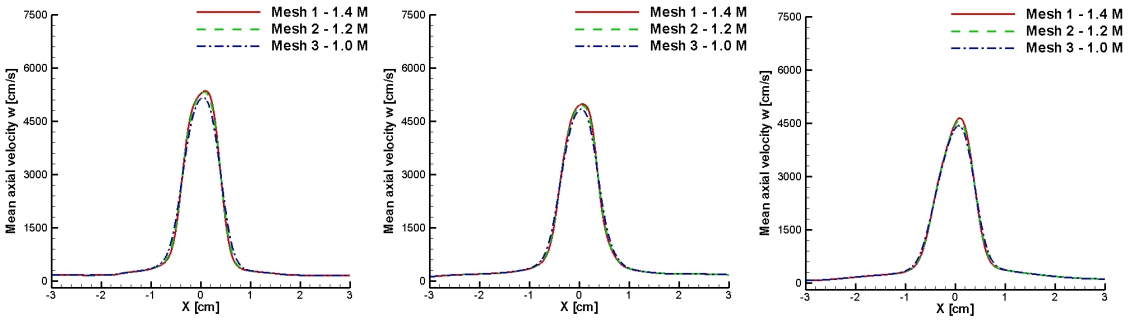

Figure 3: Mean axial velocity component profile for the three meshes at three axial locations Z = 2.0 cm (left), Z = 4.0 cm (middle) and Z = 6.0 cm (right).

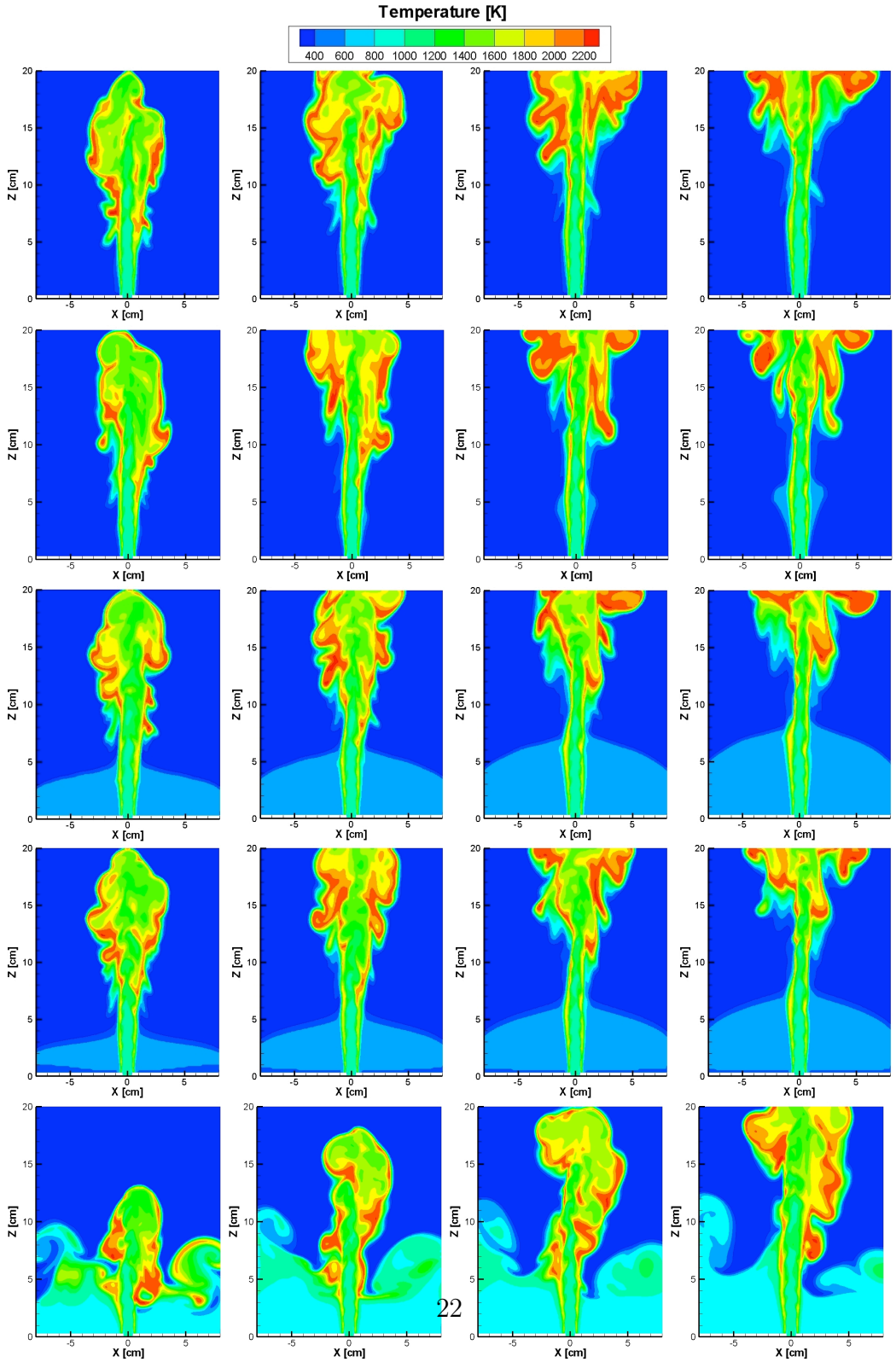

Figure 4: Cross-sectional temperature contour plots at different time instants from left to right t = 0.015s, 0.020s, 0.025s and 0.030s for Case A (top) to Case E (bottom).

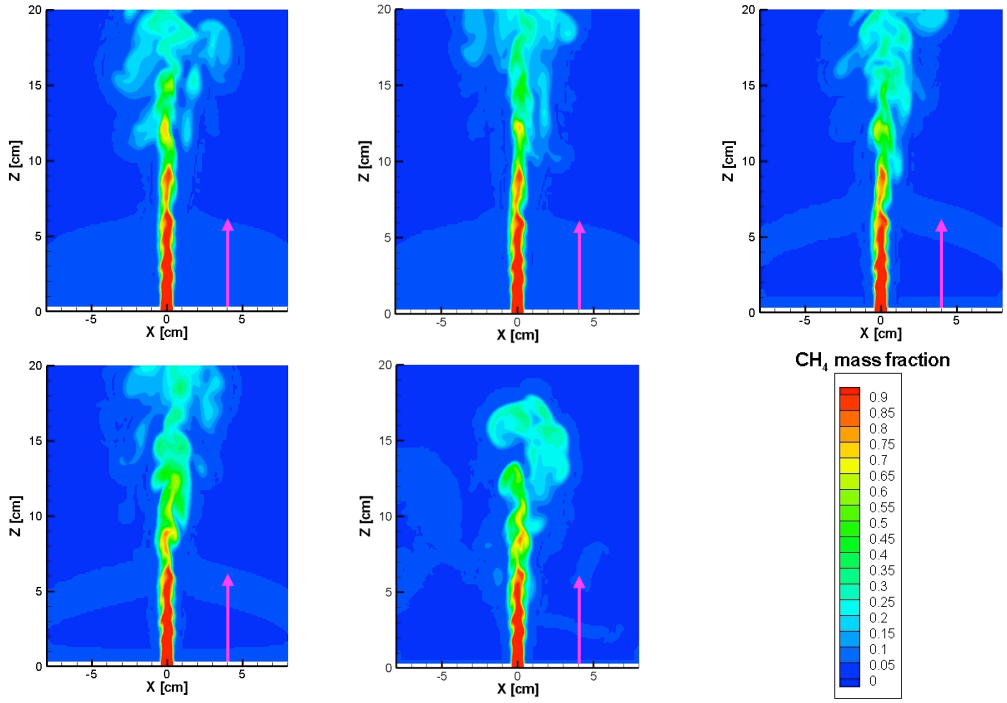

Figure 5: Cross-sectional fuel mass fraction Y_{CH_4} contour plots at time instant t = 0.020s for Cases A to Case E from left to right.

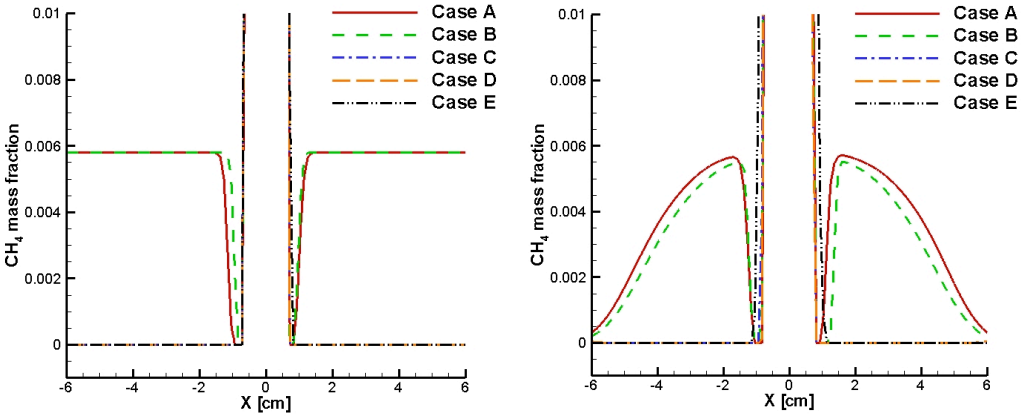

Figure 6: Zoomed profile of the methane mass fraction Y_{CH_4} at two axial locations Z = 2.0 cm (left) and Z = 4.0 cm (right).

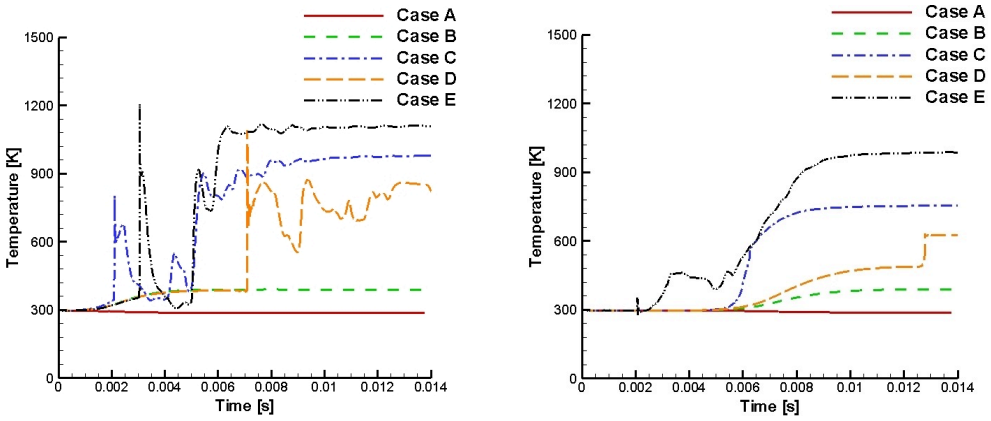

Figure 7: Timetraces of temperature of two points located in the VAM mixture P1$(3.0, 0.0, 0.5)$ (left) and P2$(5.0, 0.0, 0.5)$ (right).

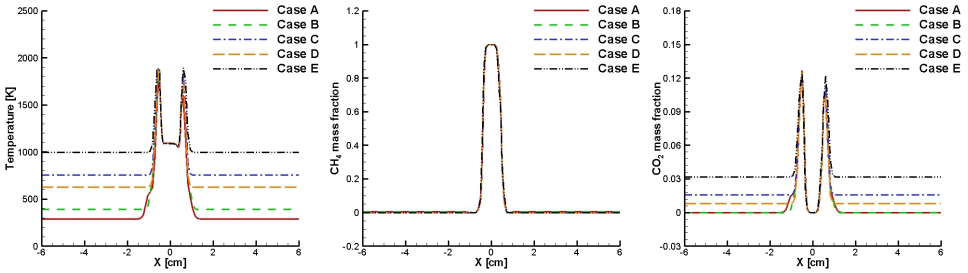

Figure 8: Radial profiles of scalars (T, CH_4 and CO_2) at the axial location Z = 2.0 cm at the time instant t = 0.020s.

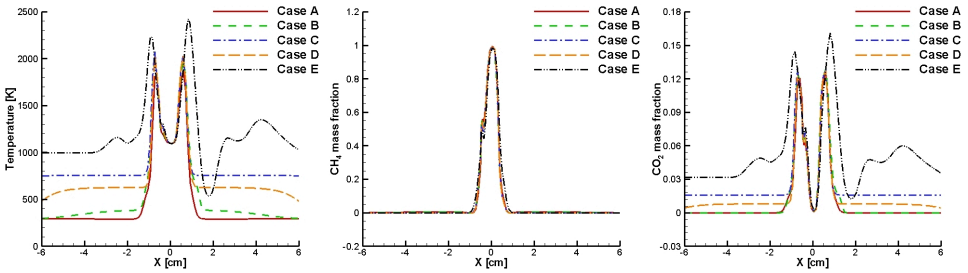

Figure 9: Radial profiles of scalars (T, CH_4 and CO_2) at the axial location Z = 4.0 cm at the time instant t = 0.020s.

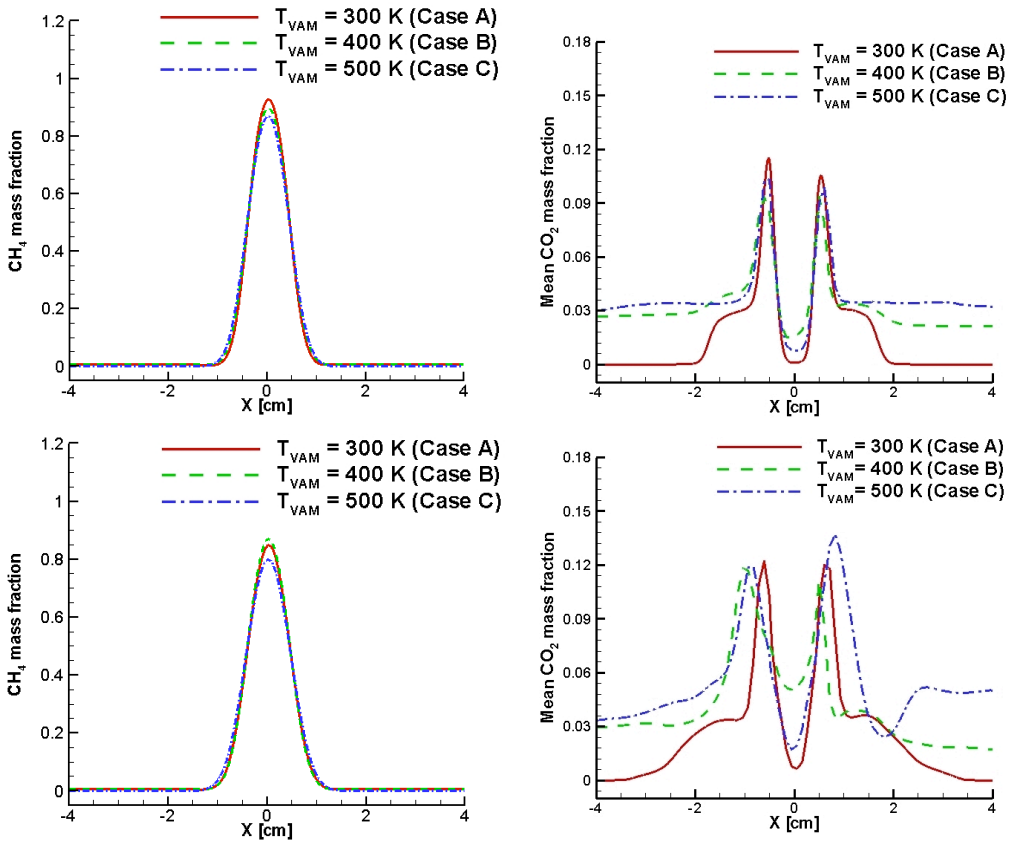

Figure 10: Time-averaged species mass fraction profiles ($\overline{Y}_{CH_4}$ and $\overline{Y}_{CO_2}$) at two axial locations Z = 2.0 cm (top) and Z = 4.0 cm (bottom).

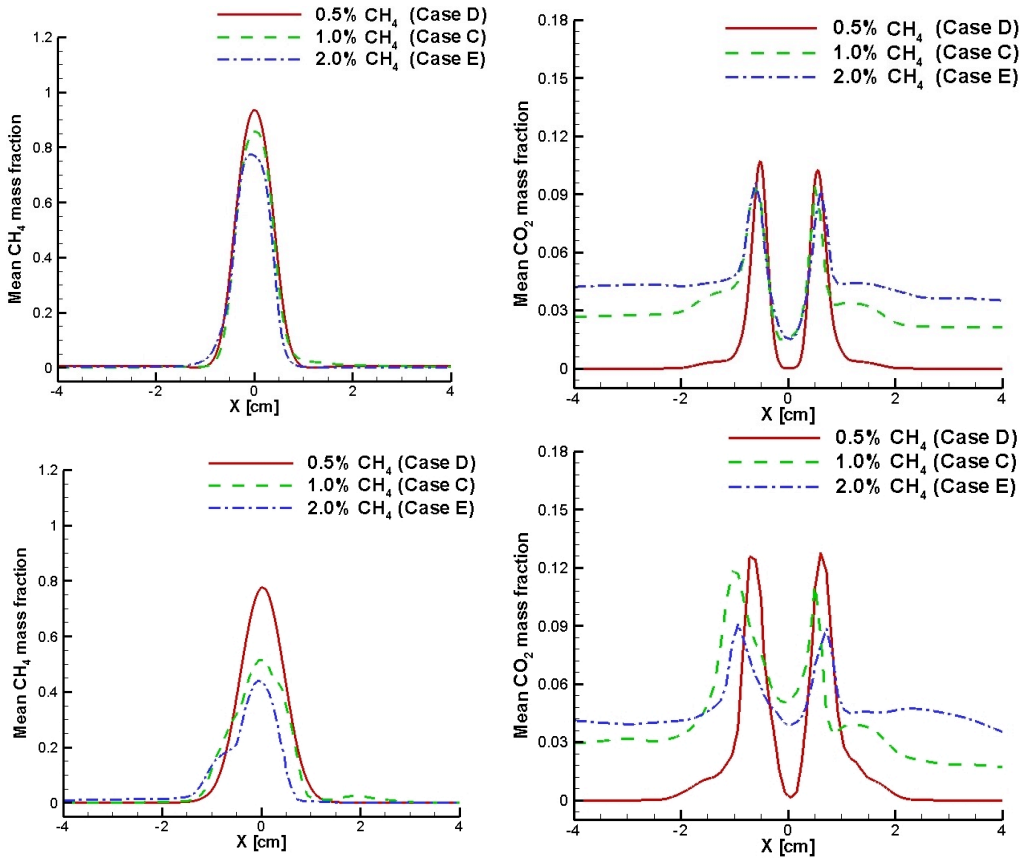

Figure 11: Time-averaged species mass fraction profiles ($\overline{Y}_{CH_4}$ and $\overline{Y}_{CO_2}$) at two axial locations Z = 2.0 cm (top) and Z = 4.0 cm (bottom).

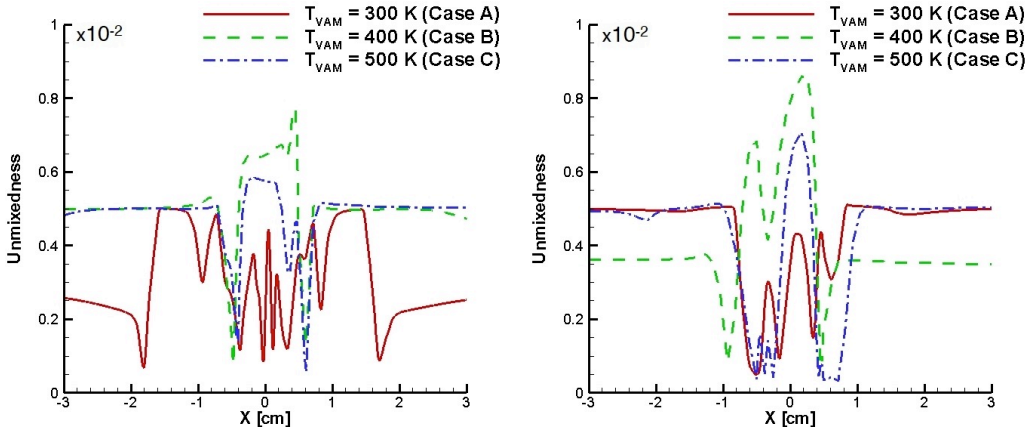

Figure 12: Radial profiles of the unmixedness at two axial locations Z = 2.0 cm (left) and Z = 4.0 cm (right).

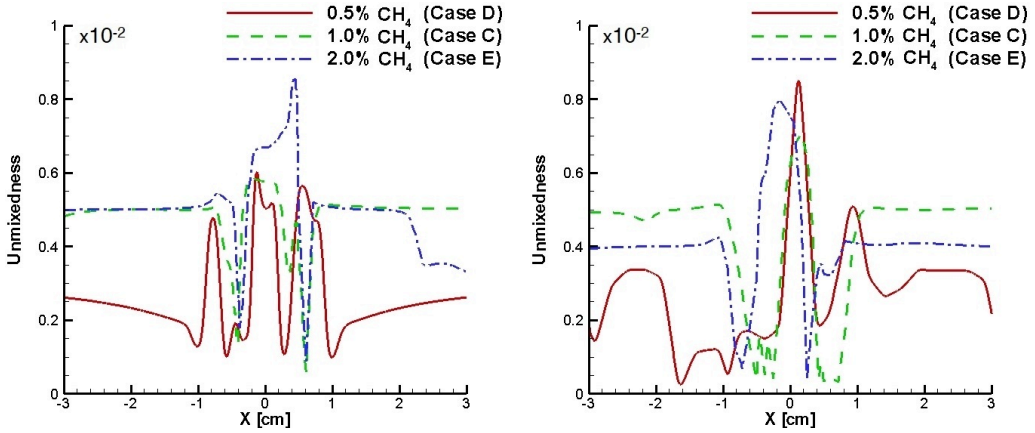

Figure 13: Radial profiles of the unmixedness at two axial locations Z = 2.0 cm (left) and Z = 4.0 cm (right).